Electronic Supplementary Information (ESI)

Title Amorphous Multinary Phyllosilicate Catalysts for Electrochemical Water Oxidation

Byunghoon Kim,[†,§] Ju Seong Kim,[†,§] Hyunah Kim[†], Inchul Park[†], Won Mo Seong[†], and Kisuk Kang[*,†,‡]*

[†]Department of Materials Science and Engineering, Research Institute of Advanced Materials (RIAM), Seoul National University, 1 Gwanak-ro, Gwanak-gu, Seoul 151-742, Republic of Korea.

[‡]Center for Nanoparticle Research, Institute for Basic Science (IBS), Seoul National University, 1 Gwanak-ro, Gwanak-gu, Seoul 151-742, Republic of Korea.

Experimental Methods

Synthesis of pristine and annealed ACFP series

The series of amorphous cobalt–iron phyllosilicates (ACFPs) were synthesized using a simple co-precipitation method. In this process, 10.7 mmol sodium metasilicate (Na_2SiO_3, Sigma-Aldrich) dissolved in 15 mL of deionized water was added to a 8 mmol mixture of cobalt chloride ($CoCl_2$, Sigma-Aldrich) and iron chloride tetrahydrate ($FeCl_2 \cdot 4H_2O$, Sigma-Aldrich) dissolved in 75 mL of deionized water under stirring for 30 min. The ratio between cobalt chloride and iron chloride tetrahydrate was varied to 10:0, 8:2, 6:4, 4:6, 2:8, and 0:10 to obtain an ACFP series with a wide range of metal compositions. To obtain crystallized ACFPs, a hydrothermal method was applied. The mixed solution described above was transferred into a sealed Teflon-lined stainless steel autoclave and heated at 180

°C for 24 h in an air atmosphere. All the precipitated solutions were washed several times with deionized water and ethanol using centrifugation and dried in a vacuum oven at 70 °C.

Synthesis of cobalt–iron oxyhydroxide series

The synthesis of the cobalt–iron oxyhydroxides was performed using homogeneous precipitation with the same metal precursors as those used for the ACFPs, hexamethylenetetramine (HMT, Sigma-Aldrich) and sodium nitrate ($NaNO_3$, Sigma-Aldrich). After dissolving 10 mmol of the metal precursor mixture, 10 mmol HMT, and 4 mmol $NaNO_3$ in 50 mL of deionized water, the solution was placed in an 80 °C vacuum oven for 24 h. After the solution became opaque as a result of the precipitation reaction, the obtained precipitate was collected using the same method described above.

Materials characterization

X-ray diffraction (D2-Phaser, Bruker) with Cu-Kα radiation was used to ascertain the crystal structure of the prepared samples. The local environments of the ACFP series were identified using Fourier-transform infrared spectroscopy (Hyperion 3000, Bruker). Quantitative analysis of the elemental composition was performed using energy dispersive spectroscopy (EDS) coupled with FE-SEM (SU70, Hitachi). The valence states of Co and Fe ions were investigated using X-ray adsorption near edge structure (XANES) spectroscopy performed at the 8C-Nano XAFS beamline at the Pohang Accelerator Laboratory (PAL). All the XANES data were measured in transmittance mode using an electron energy of 2.5 GeV and current of 400 mV in top-up mode.

Electrochemical characterization

Electrochemical tests were performed using a three-electrode beaker cell system and an electrochemical potentiostat (CHI 608C, CH Instruments) at room temperature. The working electrode was prepared using the drop-casting method. To make a homogeneous catalyst ink, 5 mg of the catalyst material was dispersed in a mixed solution of 0.1 mL of neutralized Nafion and 1 mL of deionized water

and sonicated for 30 min. The ink was uniformly dropped onto carbon fiber paper (CFP) with a mass loading of 0.4 mg cm^{-2}, and the electrode was dried in a 80 °C oven for 30 min. An Hg/HgO electrode filled with 1 M NaOH and Pt were used as the reference and counter electrode, respectively. Cyclic voltammetry (CV) data were recorded using 1 M KOH solution as an electrolyte at a scan rate of 10 mV s^{-1}, and the ohmic resistance in a beaker cell was automatically compensated using a potentiostat. The capacitive background current was corrected by averaging the forward and backward curves. The potentials of all the CV data were converted to the reversible hydrogen electrode (RHE) scale. In this paper, the overpotential (η) at the current density of 10 mA cm^{-2} was determined by subtracting 1.23 V (the thermodynamic water oxidation potential) from the measured potential (vs. RHE). A Tafel plot was constructed by plotting E (vs. RHE) against log j using the following Tafel equation: $\eta = a \log j + b$, where η is the overpotential, a is the slope, and b is a constant. To evaluate the surface areas of the prepared electrodes, the electrochemically active surface area (ECSA) was estimated using the electrochemical double-layer capacitance. The slope of the scan rate versus current density in the capacitive current region ($\Delta j = j_a - j_c$, at a potential of 1.05 V_{RHE}) was used to determine the relative value of the double-layer capacitance. A long-term stability test was conducted at j = 10 mA cm^{-2} for 24 h.

Computational details

The first-principles calculations presented in this work were performed based on spin-polarized density functional theory (DFT) using the Vienna *ab initio* simulation package (VASP).[1] The exchange-correlation energies were described within the generalized gradient approximation plus Hubbard U (GGA+U) framework parameterized using the revised Perdew−Burke−Ernzerhof (RPBE) exchange correlation functional.[2, 3] Effective Hubbard-U parameters of U_{eff}(Co) = 3.5 eV and U_{eff}(Fe) = 4.0 eV were applied to the 3d electrons of Co atoms and Fe atoms, respectively, consistent with the values reported in other works.[4-8] To depict the interactions between the valence electrons and ionic cores, the projector augmented wave (PAW) pseudopotentials were used as implemented in VASP.[9] The surface

properties of pure and Fe-substituted ACP were calculated from the five-layer slab models constructed in our previous work.[8] These slab models consisted of three metal sites per surface separated by more than 15 Å of vacuum to remove the interaction between the slabs. The atomic positions within the topmost three layers of the slab were allowed to relax below a maximum threshold force of 0.05 eV/Å within an energy cutoff of 550 eV and a 3 × 3 × 1 gamma-point-centered *k*-point mesh, consistent with our previous work on ACP. [8] Dipole moment correction was employed to eliminate the effect of residual dipole moments perpendicular to the surface.

Thermodynamics of OER

The OER process is divided into four proton-coupled electron transfer (PCET) steps in which one proton and one electron are extracted in each step. [10] According to the Brønsted–Evans–Polanyi (BEP) relation, the overall rate of the catalytic reaction is mainly determined by the thermodynamic energy differences between the catalytic states. [10-12] Therefore, we attempted to estimate the OER energies and theoretical overpotential (η) of the OER based on the acid-based mechanism proposed by Rossmeisl, Nørskov, and coworkers.[13, 14] In this mechanism, the OER is assumed to proceed according to the following four elementary reaction steps (under alkaline conditions):

$$* + 4OH^- (aq) \rightarrow OH^* + 3OH^- (aq) + e^- \quad (1)$$

$$OH^* + 3OH^- (aq) \rightarrow O^* + 2OH^- (aq) + H_2O (l) + e^- \quad (2)$$

$$O^* + 2OH^- (aq) + H_2O (l) \rightarrow OOH^* + OH^- (aq) + H_2O (l) + e^- \quad (3)$$

$$OOH^* + OH^- (aq) + H_2O (l) \rightarrow O_2 (g) + 2\ H_2O (l) + * + e^-, \quad (4)$$

where * denotes a surface adsorption site.

During the OER cycle, the intermediates of OH*(step 1), O* (step 2), and OOH* (step 3) are formed in turn. The Gibbs free energy differences for steps (1)–(4) are calculated according to the following equations:

$$\Delta G_1 = \Delta G_{OH*} - eU + \Delta G_{H+}(pH) \quad (5)$$

$$\Delta G_2 = \Delta G_{O*} - \Delta G_{OH*} - eU + \Delta G_{H+}(pH) \quad (6)$$

$$\Delta G_3 = \Delta G_{OOH*} - \Delta G_{O*} - eU + \Delta G_{H+}(pH) \quad (7)$$

$$\Delta G_4 = 4.92 - \Delta G_{OOH*} - eU + \Delta G_{H+}(pH), \quad (8)$$

where U is the potential measured against the normal hydrogen electrode (NHE) at standard conditions. The Gibbs free energy change of a proton relative to the NHE at non-zero pH is represented by the Nernst equation as $\Delta G_{H+}(pH) = -k_B T \ln(10) \times pH$. To avoid the calculation involving O_2 gas, which is not precisely predictable within the GGA-DFT scheme, the sum of ΔG_{1-4} was fixed at 4.92 eV, the negative of the experimental Gibbs free energy of the formation of two water molecules ($2H_2O \rightarrow 2H_2 + O_2$).[14] The ΔG_{OH*}, ΔG_{O*}, and ΔG_{OOH*} terms in Equation (5)–(8) were determined by the adsorption energies of each intermediate, i.e., OH*, O*, and OOH*. The adsorption energies of the intermediates were calculated from the DFT energy (E_i), zero-point energy (ZPE), and entropy correction using $\Delta G_i = \Delta E_i + \Delta ZPE - T\Delta S$. The energy difference ΔE_i was estimated relative to those of H_2O and H_2 at the computational standard hydrogen electrode (SHE), i.e., $U = 0$ and pH = 0, as

$$\Delta E_{OH*} = E_{OH*} - E_* - [E(H_2O) - \frac{1}{2}E(H_2)] \quad (9)$$

$$\Delta E_{O*} = E_{O*} - E_* - [E(H_2O) - E(H_2)] \quad (10)$$

$$\Delta E_{OOH*} = E_{OOH*} - E_* - \left[2E(H_2O) - \frac{3}{2}E(H_2)\right]. \quad (11)$$

Among the four elementary steps, the step requiring the highest reaction free energy is the potential-determining step (PDS). Thus, the theoretical η was determined using

$$\eta = \max[\Delta G_1, \Delta G_2, \Delta G_3, \Delta G_4]/e - 1.23\ [V]$$

Table S1. Ratios of elements in the ACFP series measured using EDS.

	Co (at.%)	Fe (at.%)	Si (at.%)	O (at.%)
ACP	16.589		18.605	64.8055
ACFP82	12.31	3.28	17.945	66.47
ACFP64	9.79	6.735	18.785	64.69
ACFP46	5.815	9.07	17.755	67.355
ACFP28	2.61	10.595	16.205	70.59
AFP		16.47	18.12	65.41

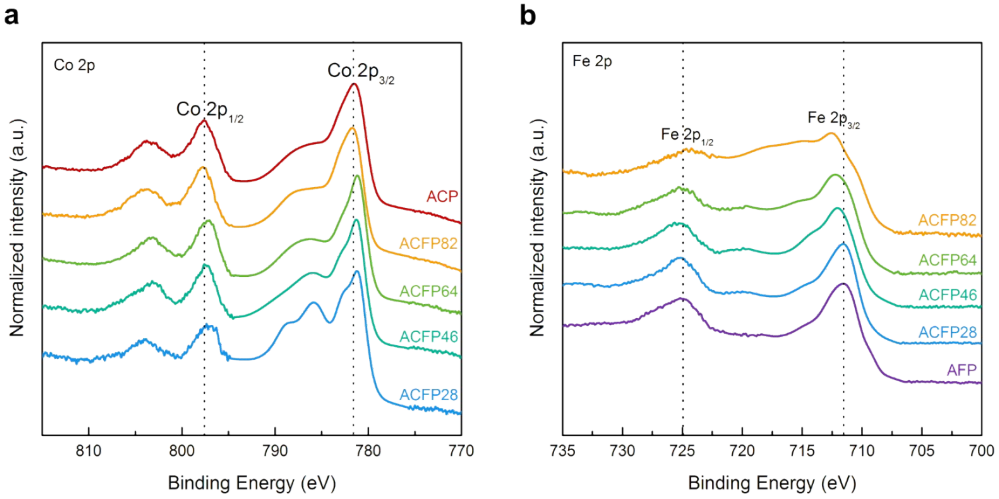

Figure S1. X-ray photoelectron spectroscopy (XPS) analysis of ACFP samples around (a) the Co 2p and (b) the Fe 2p binding energy regions. The characteristic Co $2p_{1/2}$ and $2p_{3/2}$ peaks in the spectra of ACP, and Fe $2p_{1/2}$ and $2p_{2/3}$ peaks in the spectra of AFP indicates Co^{2+} and Fe^{3+} signals, respectively.[15-17] Only slight shifts of such peaks are observed for both Co and Fe spectra in the entire composition of ACFP series. This indicates that the valence states of surficial Co and Fe ions are close to +2 and +3, respectively, in ACFPs irrespective of Co:Fe ratios.

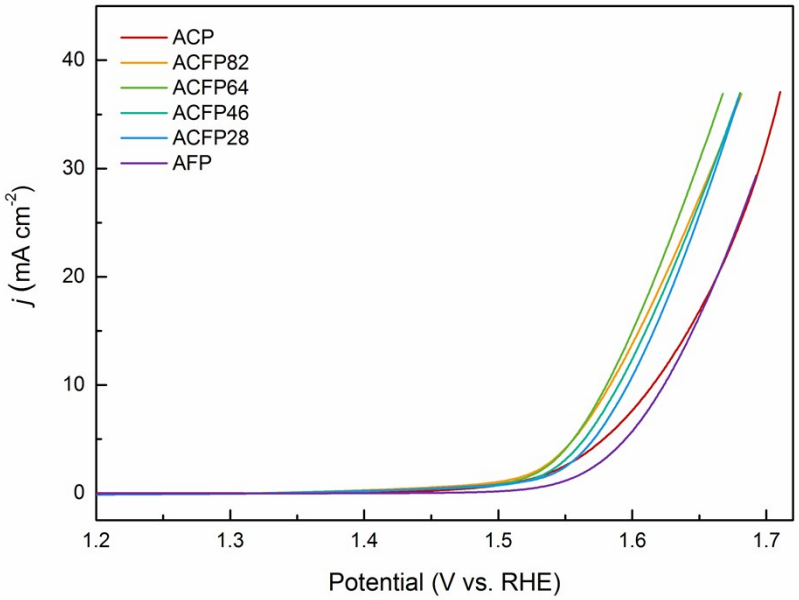

Figure S2. OER polarization curves of ACFP samples measured without *iR*-compensation.

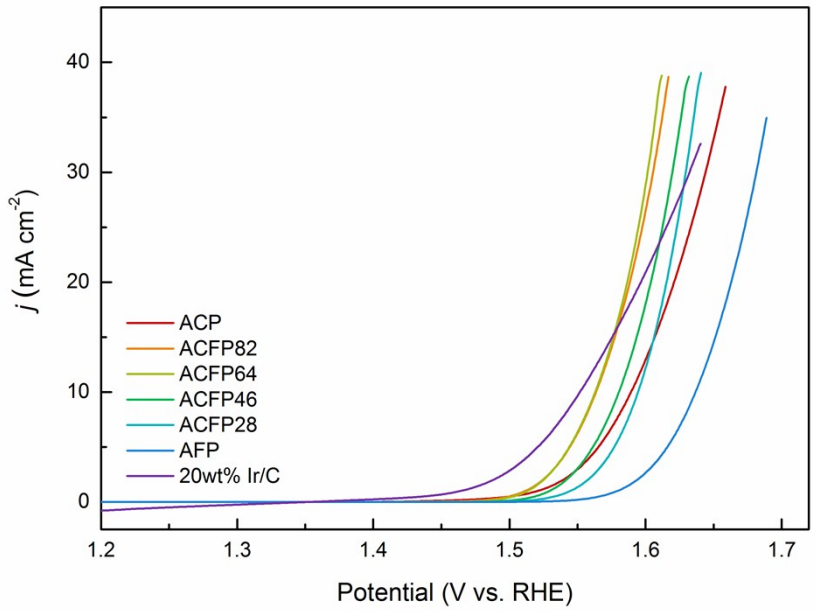

Figure S3. *iR*-corrected polarization curves of the benchmark iridium oxide sample (20wt% Ir/C) and ACFP samples. All curves were obtained in 1M KOH at a scan rate of 10 mV s^{-1}. At a current density of 10 mA cm^{-2}, Ir/C sample exhibits η of 322 mV, slightly lower than ACFP samples. Nonetheless, the polarization curves of ACFPs show steeper slopes than that of Ir/C, suggesting the greater OER properties of ACFPs at a high current density region (>20 mA cm^{-2}). The comparisons of OER properties with more various benchmark catalysts are tabulated in Table S2.

Table S2. The comparison of the OER parameters between ACFP samples and benchmark OER catalysts.

Catalysts	Electrolyte	Substrate	Overpotential (mV)	Reference
ACFP 64	1 M KOH	Carbon fiber paper	329 at 10 mA cm^{-2}	This work
Iridium oxide (20wt% Ir/C)	1 M KOH	Carbon fiber paper	322 at 10 mA cm^{-2}	This work
RuO_2	0.1 M deoxygenated $HClO_4$	Fluorine-doped tin oxide	130 (onset)	18
Layered-structure family				
NiOOH	0.1 M KOH/LiOH	PtO/AuO	375 at 10 mA cm^{-2}	19
NiFe-LDH	1 M KOH	Glassy carbon electrode	300 at 10 mA cm^{-2}	20
Ni-Co hydroxide nanotube array	0.1M KOH	Indium tin oxide	730 at 10 mA cm^{-2}	21
CoCr-LDH	0.1 M KOH	Glassy carbon electrode	340 at 10 mA cm^{-2}	22
Ultrathin Co-Mn LDH	1M KOH	Glassy carbon electrode	324 at 10 mA cm^{-2}	23
Spinel family				
$CoFe_2O_4$	0.1 M KOH	Glassy carbon electrode	370 at 10 mA cm^{-2}	24
Co_3O_4	1 M KOH	Au	400 at 10 mA cm^{-2}	25
$NiFe_2O_4$	1 M KOH	Carbon paper	360 at 10 mA cm^{-2}	26
Perovskite family				
$Ba_{0.5}Sr_{0.5}Co_{0.8}Fe_{0.2}O_3$	0.1 M KOH	Glassy carbon electrode	250 at 0.05 mA cm^{-2}	27
$BaNi_{0.83}O_{2.6}$	0.1 M KOH	Glassy carbon electrode	270 at 0.05 mA cm^{-2}	28
$CaFeO_3$	0.1 M KOH	Glassy carbon electrode	390 at 10 mA cm^{-2}	29
Amorphous structure				
CoP_i	0.1 M KP_i	Indium tin oxide	410 at 1 mA cm^{-2}	15
Fe–Co–W oxyhydroxide (1:1.02:0.70)	0.1 M KOH	Gold plated Ni foam	191 at 10 mA cm^{-2}	30

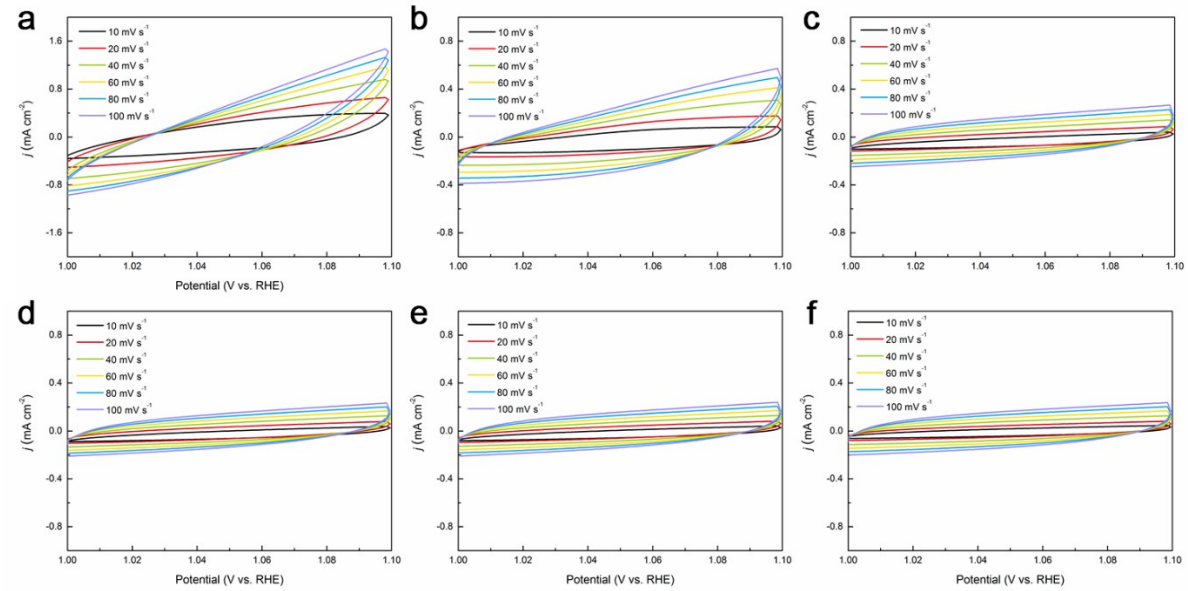

Figure S4. CV curves of (a) ACP, (b) ACFP82, (c) ACFP64, (d) ACFP46, (e) ACFP 28, and (f) AFP in 1 M KOH electrolyte as a function of scan rate, enabling the evaluation of the relative electrochemical active surface area (ECSA). The ECSA was used as an indicator of the relative surface area of each electrode to exclude the contribution of the surface area on the catalytic activity. The ECSA was determined from its proportional relation to the double-layer capacitance (C_{dl}); thus, the C_{dl} -values of the ACFPs were measured using CV. The C_{dl} values were obtained by estimating the slope of the scan rate with respect to the capacitive current, as shown in Figure S5.

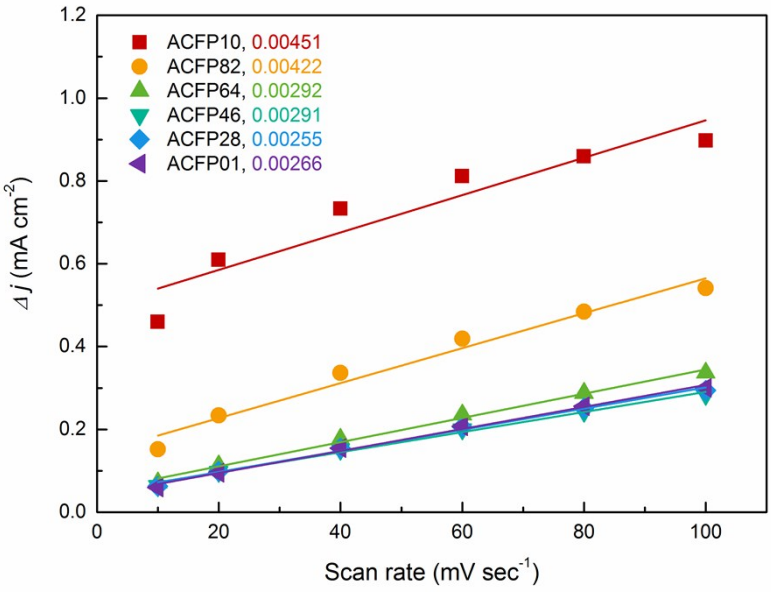

Figure S5. $\Delta j = j_a - j_c$ at 1.05 V vs. RHE as a function of the scan rate to evaluate C_{dl}. The slopes of plots are 0.00451, 0.00422, 0.00292, 0.00291, 0.00255, and 0.00266 for ACP, ACFP82, ACFP64, ACFP46, ACFP 28, and AFP, respectively.

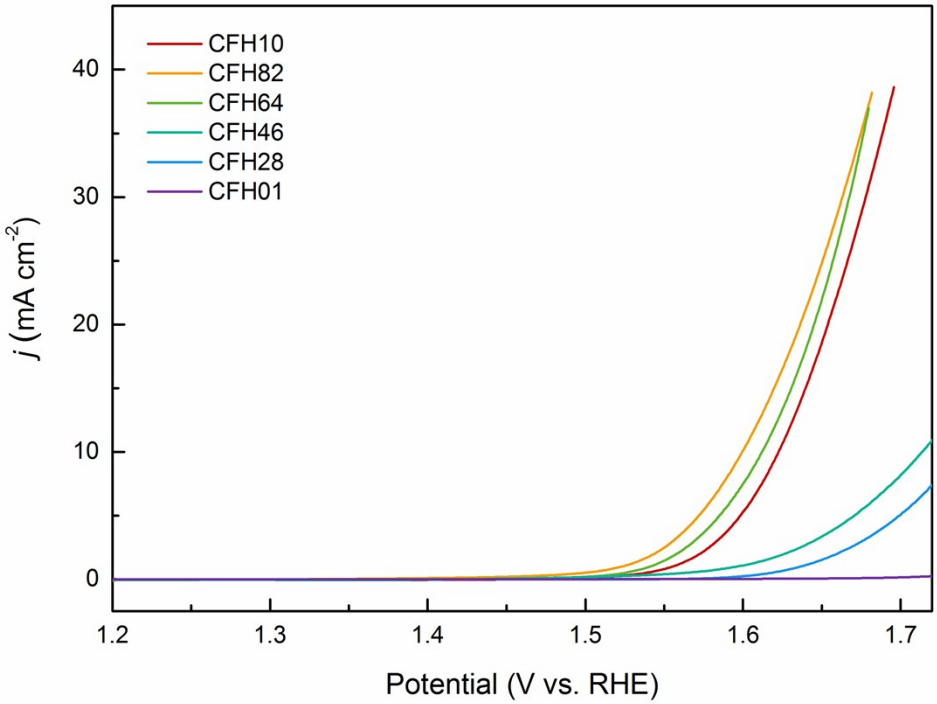

Figure S6. *iR*-corrected polarization curves of Co–Fe hydroxide series in 1 M KOH at a scan rate of 10 mV s^{-1}.

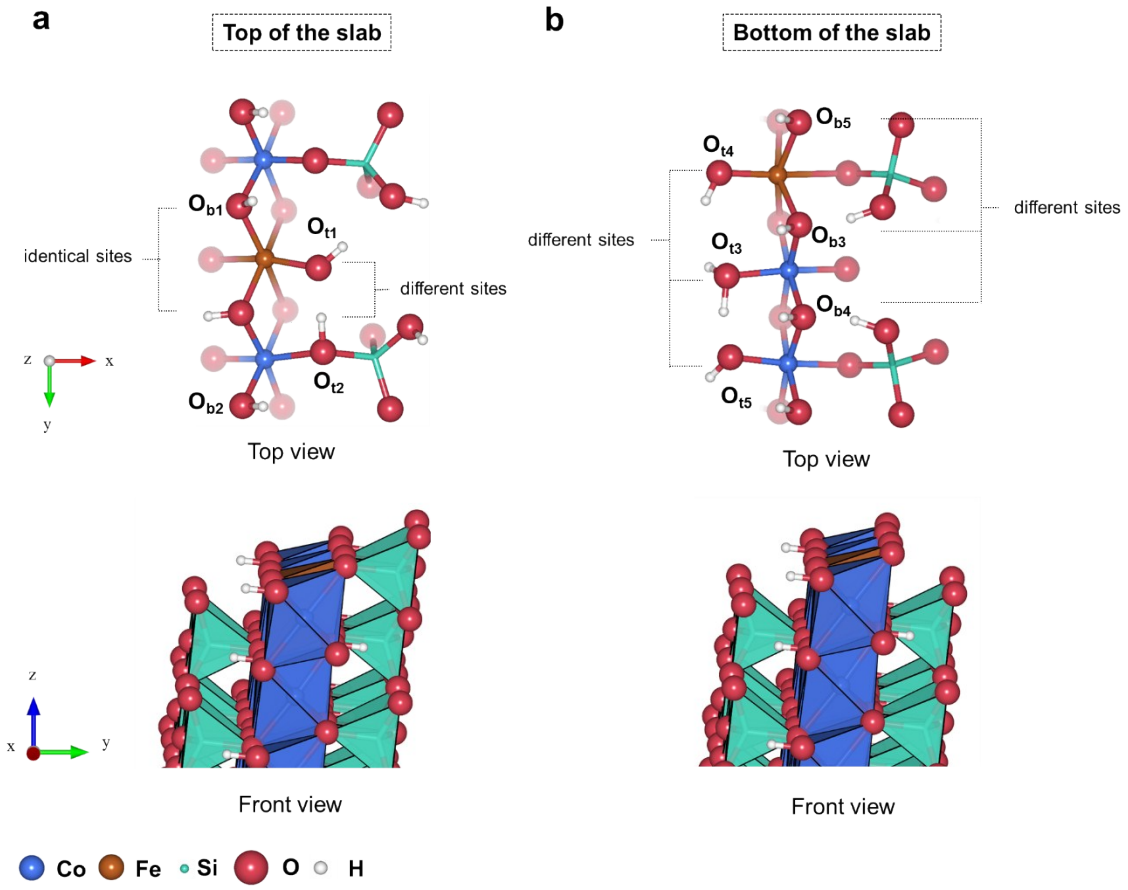

Figure S7. Surface structure of Fe-substituted ACP slab. Because of the asymmetry of the slab model, there are two types of surface layers depending on the orientation of the silicate groups: **(a)** top layer of the slab (model 1) and **(b)** bottom layer of the slab (model 2). The oxygen reaction sites that were considered for the OER mechanism analysis are indicated as "O_t" or "O_b". Only the topmost atoms are shown for improved clarity.

Figure S7 shows the surface structure of the Fe-substituted ACP slab. In our previous work, the structural motif of the ACP with Co:Si:O = 1:1:4 was predicted based on DFT calculations.[8] Furthermore, we cleaved the ACP to form the five-layer slab model having similar atomic configurations as the $(10\bar{1}4)$ surface of CoOOH, which is known to be the most OER-active surface for cobalt oxyhydroxides (see Ref. 8 for more details on the pure ACP slab model construction).[6, 8]

Because of the asymmetry of the ACP slab, there are two types of surface layers that differ in the orientation of the silicate group on the surface. One is the top layer of the ACP slab designated as model 1 (Figure S7a), and the other is the bottom layer of the ACP slab designated as model 2 (Figure S7b).

For comparison of the OER properties between pure and Fe-substituted ACP, we substituted one of the Co ions in the established ACP slab model with an Fe ion. All the possible transition metal sites in the surface layer were considered for Fe substitution, and the most thermodynamically stable case was adopted in each model for the OER mechanism analysis (see Figure S8 and Figure S14). The presence of silicate groups and Fe ions induces the formation of diverse atomic sites with distinct local environments on the surface. As a result, the Fe-substituted ACP surface contains various surficial oxygen sites where the OER can occur. The terminal oxygen sites (denoted as O_t) indicate surficial oxygens bound to only one metal. In contrast, the bridge oxygen sites (denoted as O_b) indicate μ_2-O bridges interconnecting two transition metal ions. We considered all the possible surficial oxygen reaction sites for the OER mechanism analysis. In addition, their OER activities were compared with those of equivalent sites in the pure ACP slab. The terminal sites 1–5 and bridge sites 1–5 considered in the calculation are explicitly shown in Figure S7.

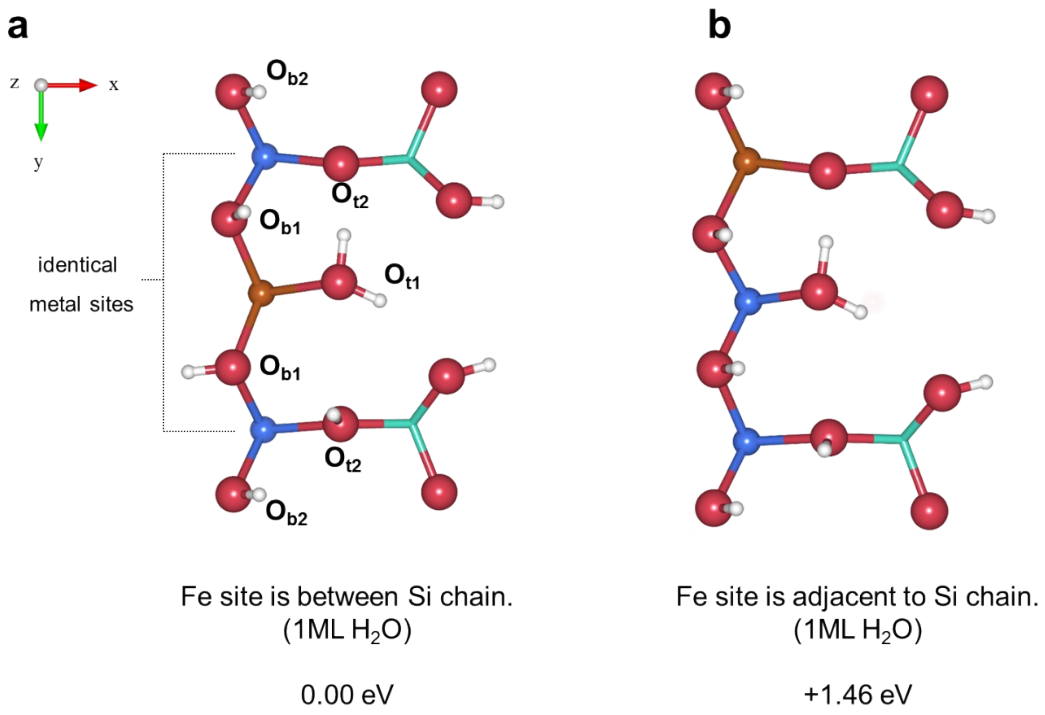

Figure S8. Result of calculation to determine Fe substitution site for the top layer of the slab model (model 1). The model in which Fe replaces the Co site between Si chains (a) is 1.46 eV more stable than the model in which Fe replaces the Co site neighboring the Si chain (b). Thus, the former was selected as the model representing the Fe substitution site. The blue, brown, green, red, and white spheres represent Co, Fe, Si, O, and H atoms, respectively. Only the topmost atoms are shown for improved clarity.

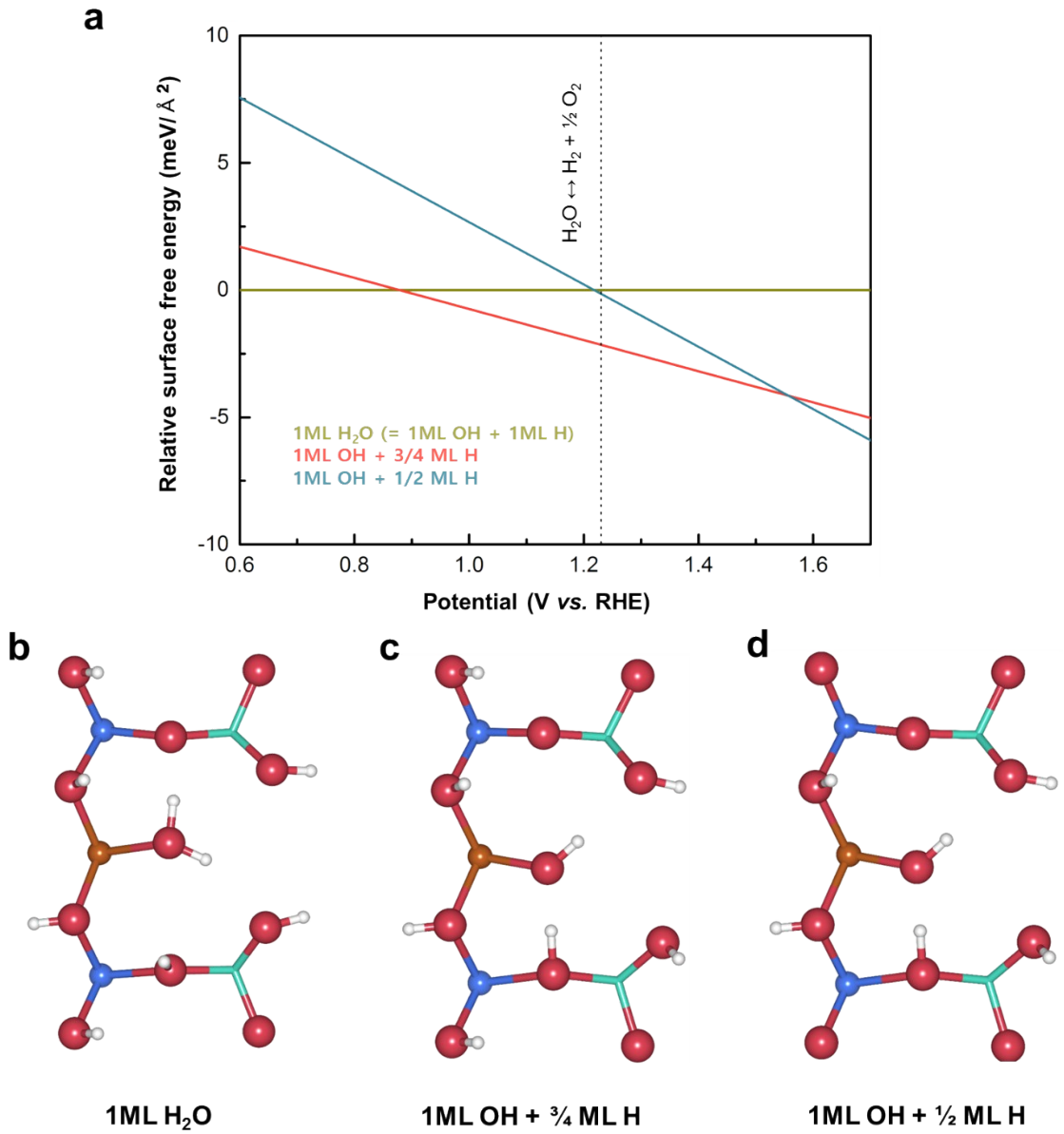

Figure S9. Surface coverage of the Fe-substituted ACP surface (model 1) corresponding to the applied potential. (a) Surface phase diagram representing relative surface free energy as a function of applied potential. The most stable surface structure with adsorbates corresponding to the applied potential is as follows: (b) 1 monolayer (ML) of co-adsorbed H_2O (below 0.89 V), (c) 1 ML of OH and 3/4 ML of H (from 0.89 V to 1.56 V), (d) 1 ML of OH and 1/2 ML of H (above 1.56 V). The blue, brown, green, red, and white spheres represent Co, Fe, Si, O, and H atoms, respectively. Only the topmost atoms are shown for improved clarity.

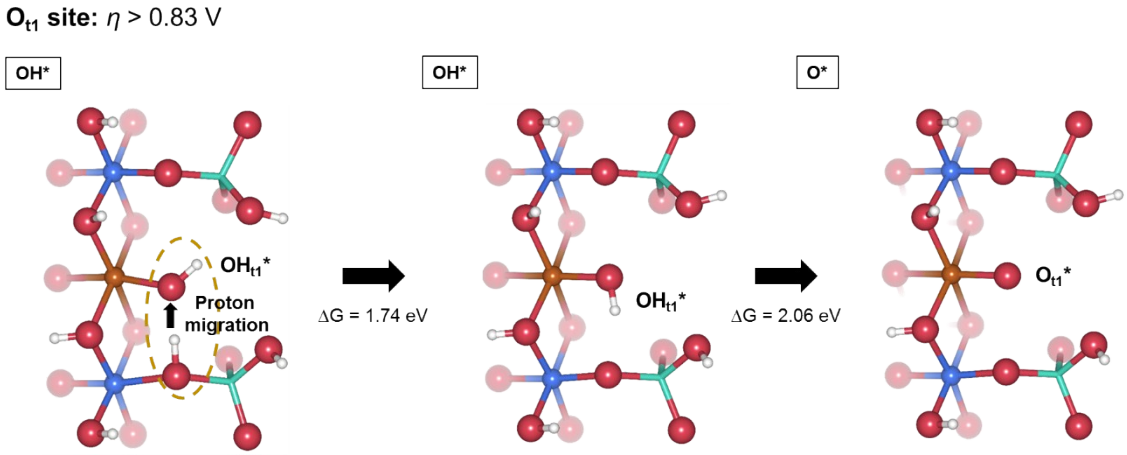

Figure S10. OER pathways and calculated OER energies for terminal site 1 on the Fe-substituted ACP surface (model 1). The OER cycle at terminal site 1 commences by the deprotonation of the terminal OH group, which requires 1.74 eV of reaction free energy. However, one proton migrates from the neighboring oxygen site to terminal site 1 during this process. Thus, further deprotonation is required to form the terminal oxo group (O*) where the nucleophilic attack of water can occur. The second deprotonation from terminal site 1 to form the O* state requires a reaction free energy of 2.06 eV, signifying that the η for the OER is greater than 0.83 V. The blue, brown, green, red, and white spheres represent Co, Fe, Si, O, and H atoms, respectively. Only the topmost atoms are shown for improved clarity.

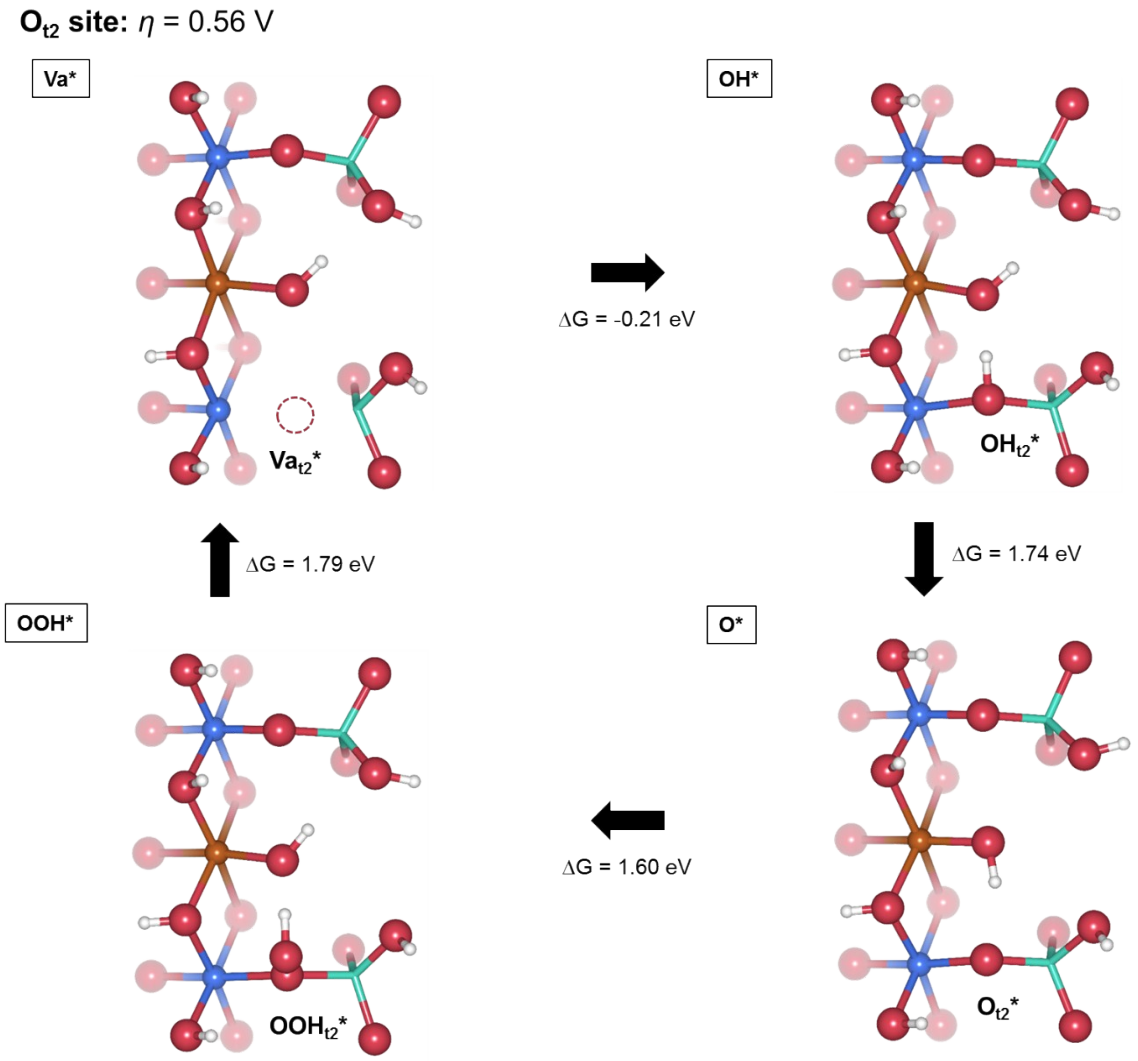

Figure S11. OER pathways and calculated OER energies for terminal site 2 on the Fe-substituted ACP surface (model 1). The step in which oxygen gas is released from the OOH group is predicted to be the potential-determining step during the OER cycle for terminal site 2. Thus, the theoretical η estimated for terminal site 2 is 0.56 V. The blue, brown, green, red, and white spheres represent Co, Fe, Si, O, and H atoms, respectively. Only the topmost atoms are shown for improved clarity.

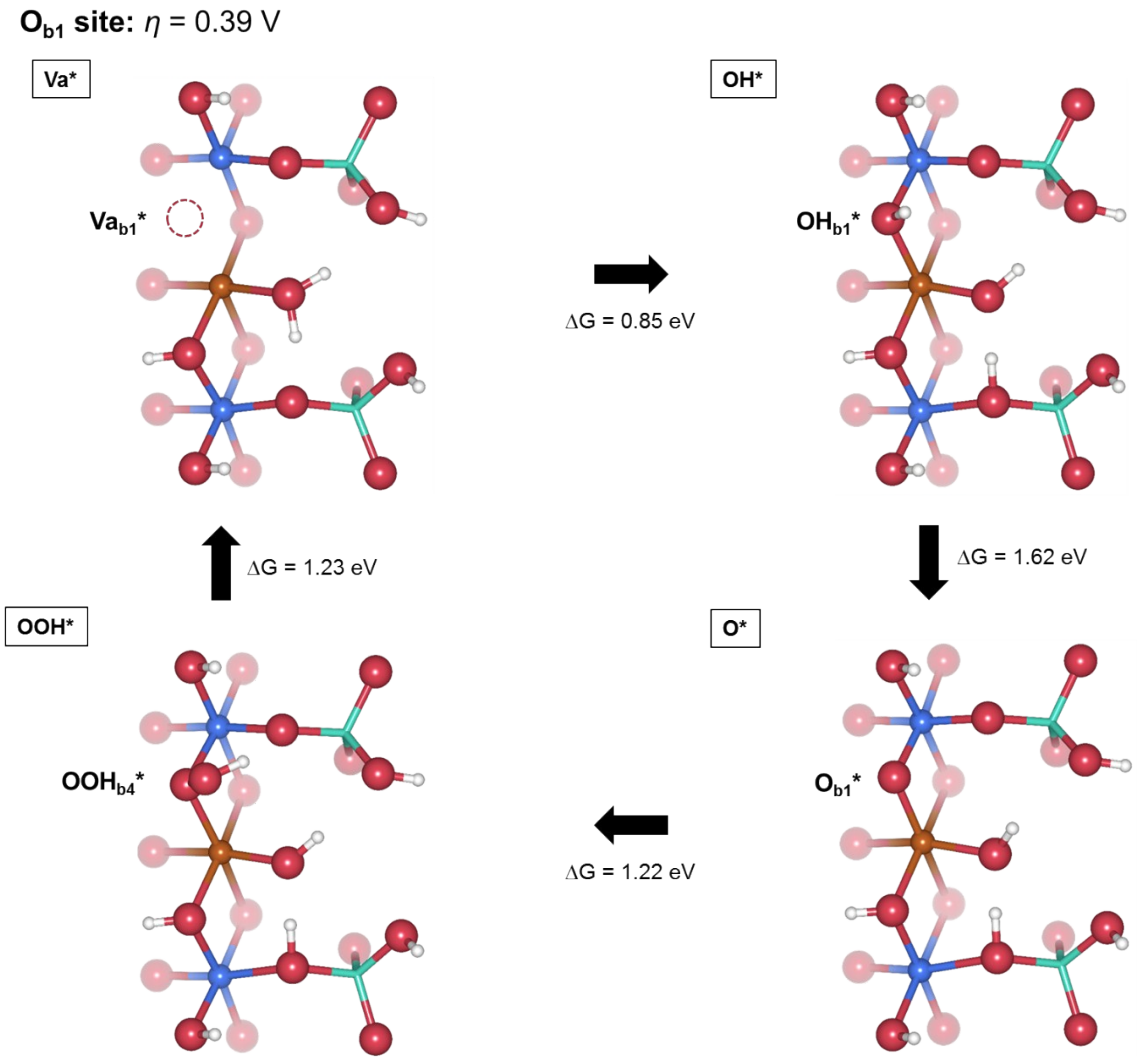

Figure S12. OER pathways and calculated OER energies for bridge site 1 on the Fe-substituted ACP surface (model 1). The PCET step from the OH* to O* state is predicted to be the potential-determining step during the OER cycle for bridge site 1. Thus, the theoretical η estimated for bridge site 1 is 0.39 V. The blue, brown, green, red, and white spheres represent Co, Fe, Si, O, and H atoms, respectively. Only the topmost atoms are shown for improved clarity.

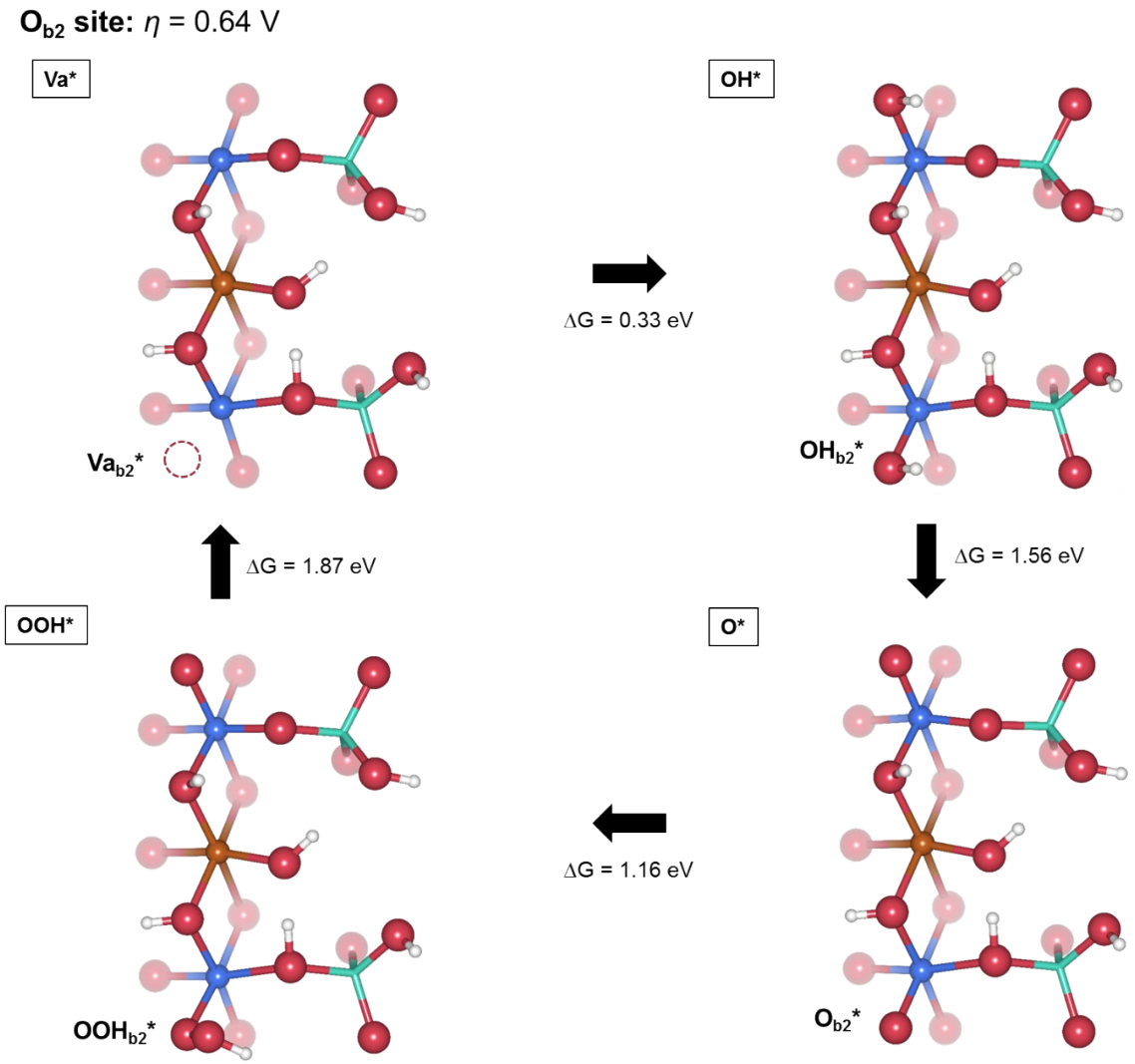

Figure S13. OER pathways and calculated OER energies for bridge site 2 on the Fe-substituted ACP surface (model 1). The step in which oxygen gas is released from the OOH group is predicted to be the potential-determining step during the OER cycle for bridge site 2. Thus, the theoretical η estimated for bridge site 2 is 0.64 V. The blue, brown, green, red, and white spheres represent Co, Fe, Si, O, and H atoms, respectively. Only the topmost atoms are shown for improved clarity.

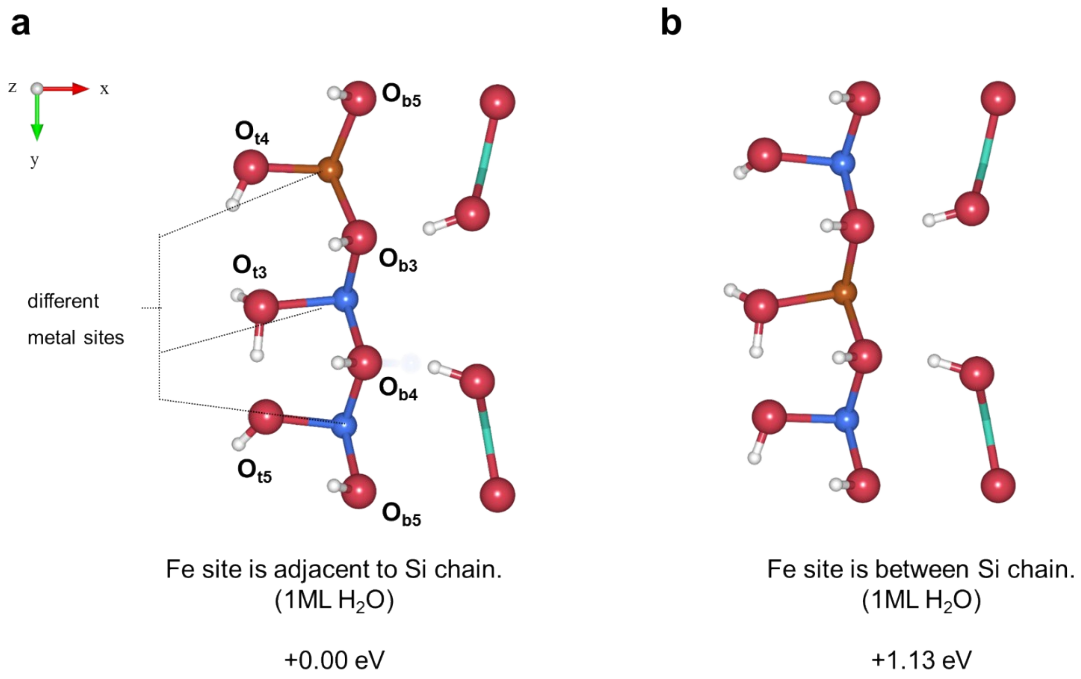

Figure S14. Result of calculation to determine Fe substitution site for the bottom layer of the slab model (model 2). The model in which Fe replaces the Co site neighboring the Si chain (a) is 1.13 eV more stable than the model in which Fe replaces the Co site between Si chains (b). Thus, the former was selected as a model representing the Fe substitution site. The blue, brown, green, red, and white spheres represent Co, Fe, Si, O, and H atoms, respectively. Only the topmost atoms are shown for improved clarity.

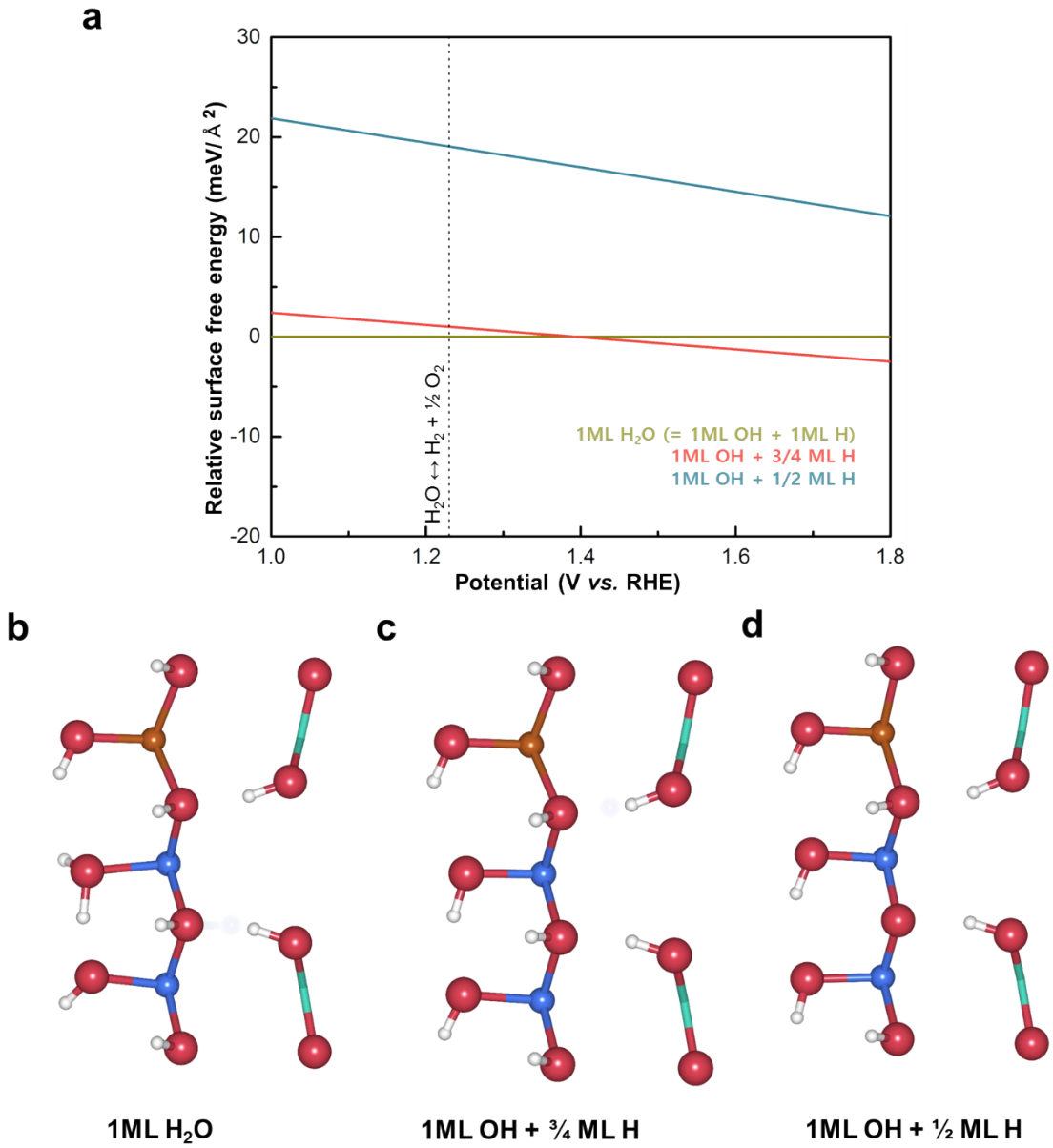

Figure S15. Surface coverage of the Fe-substituted ACP surface (model 2) corresponding to the applied potential. (a) Surface phase diagram representing relative surface free energy as a function of applied potential. The most stable surface structure with adsorbates corresponding to the applied potential is as follows: (b) 1 ML of co-adsorbed H_2O (below 1.39 V), (c) 1 ML of OH and 3/4 ML of H (from 1.39 V to 4.20 V), (d) 1 ML of OH and 1/2 ML of H (above 4.20 V). The blue, brown, green, red, and white spheres represent Co, Fe, Si, O, and H atoms, respectively. Only the topmost atoms are shown for improved clarity.

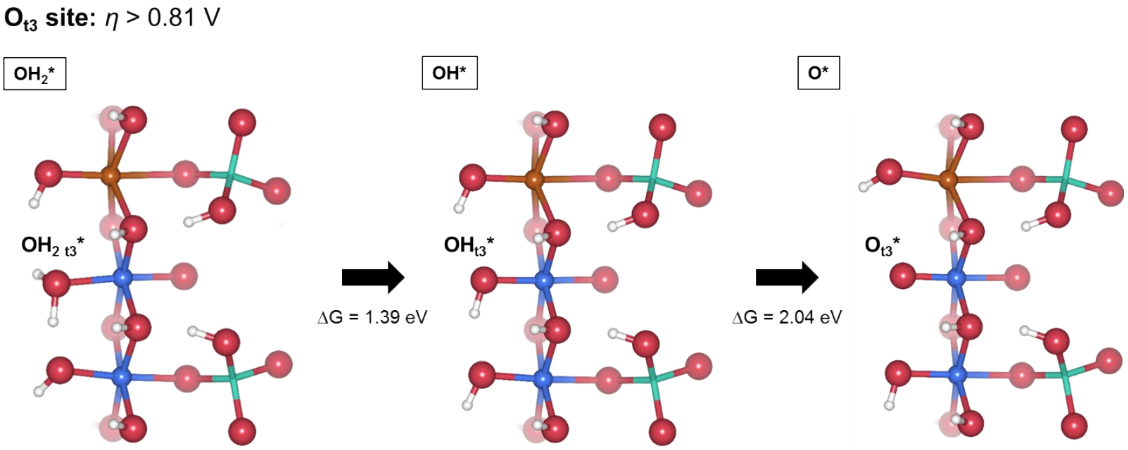

Figure S16. OER pathways and calculated OER energies for terminal site 3 on the Fe-substituted ACP surface (model 2). The formation of the oxo group (O* state) on terminal site 3 requires the removal of two protons. The second deprotonation step (OH* → O* step) requires a reaction free energy of 2.04 eV, signifying that the η for the OER is greater than 0.81 V. The blue, brown, green, red, and white spheres represent Co, Fe, Si, O, and H atoms, respectively. Only the topmost atoms are shown for improved clarity.

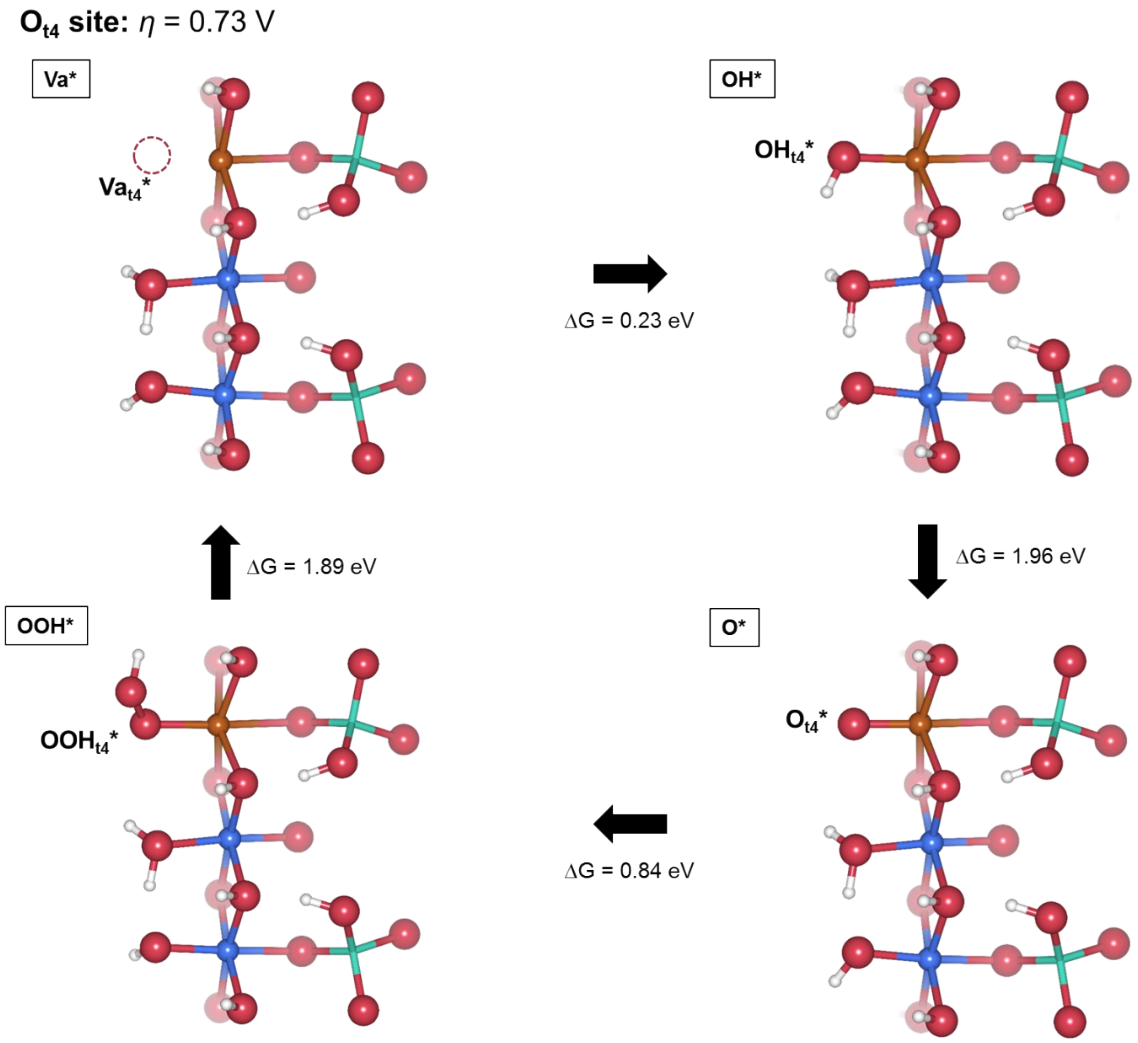

Figure S17. OER pathways and calculated OER energies for terminal site 4 on the Fe-substituted ACP surface (model 2). The PCET step from the OH* to O* state is predicted to be the potential-determining step during the OER cycle for terminal site 4. Thus, the theoretical η estimated for terminal site 4 is 0.73 V. The blue, brown, green, red, and white spheres represent Co, Fe, Si, O, and H atoms, respectively. Only the topmost atoms are shown for improved clarity.

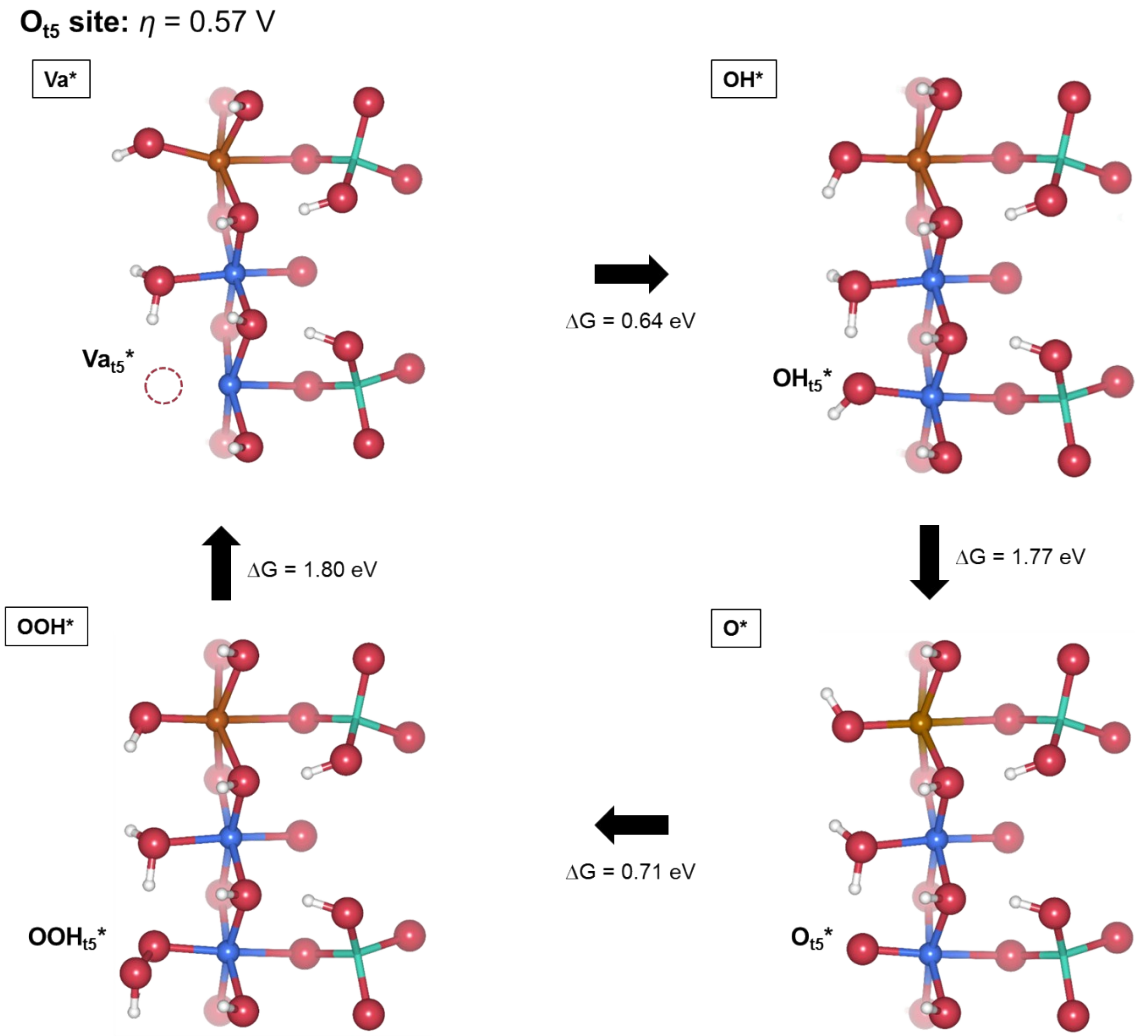

Figure S18. OER pathways and calculated OER energies for terminal site 5 on the Fe-substituted ACP surface (model 2). The step in which oxygen gas is released from the OOH group is predicted to be the potential-determining step during the OER cycle for terminal site 5. Thus, the theoretical η estimated for terminal site 5 is 0.57 V. The blue, brown, green, red, and white spheres represent Co, Fe, Si, O, and H atoms, respectively. Only the topmost atoms are shown for improved clarity.

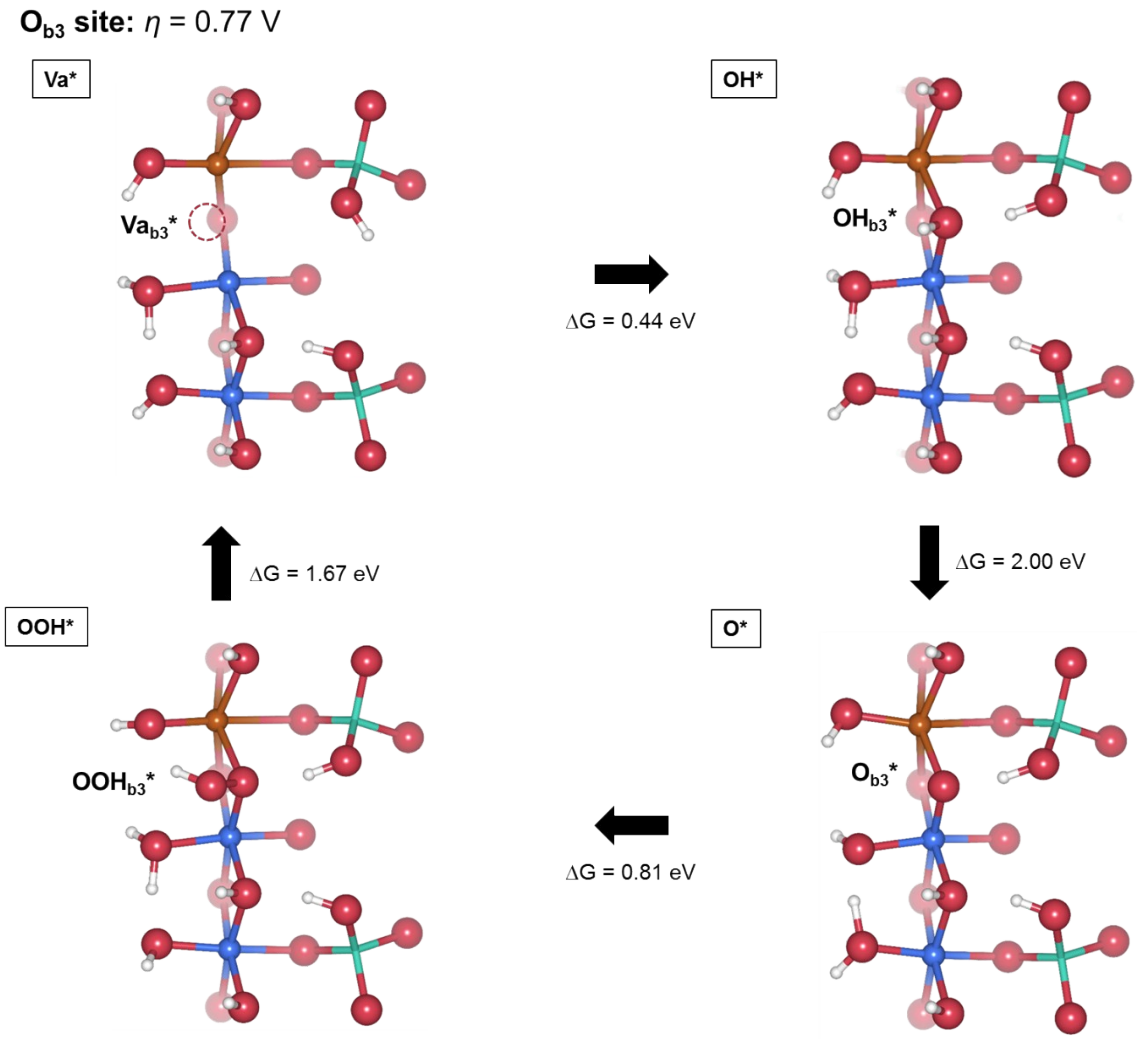

Figure S19. OER pathways and calculated OER energies for bridge site 3 on the Fe-substituted ACP surface (model 2). The PCET step from the OH* to O* state is predicted to be the potential-determining step during the OER cycle for bridge site 3. Thus, the theoretical η estimated for bridge site 3 is 0.77 V. The blue, brown, green, red, and white spheres represent Co, Fe, Si, O, and H atoms, respectively. Only the topmost atoms are shown for improved clarity.

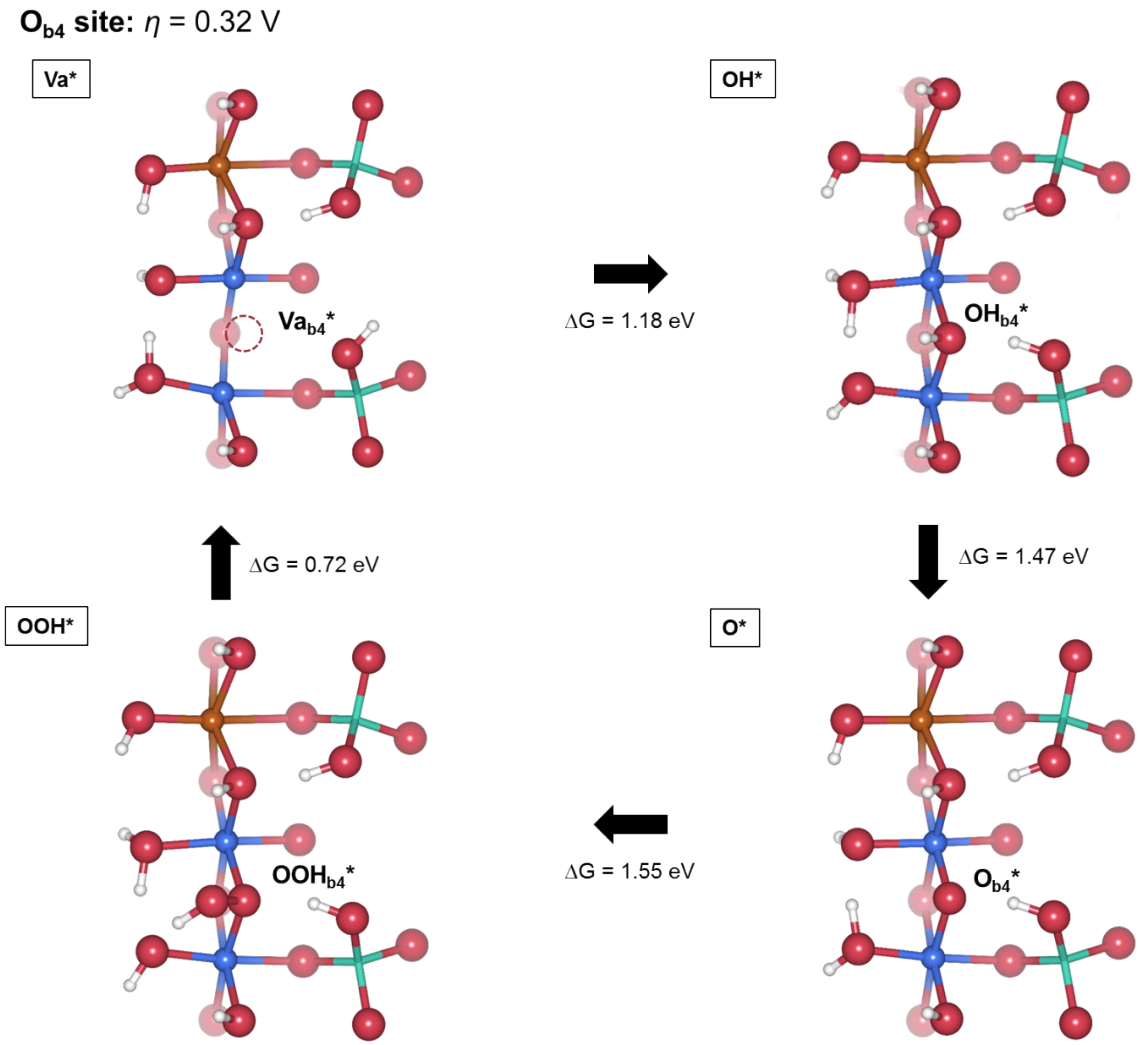

Figure S20. OER pathways and calculated OER energies for bridge site 4 on the Fe-substituted ACP surface (model 2). The step in which the nucleophilic attack of water at the oxo group occurs to form an O–O bond is predicted to be the potential-determining step during the OER cycle for bridge site 4. Thus, the theoretical η estimated for bridge site 4 is 0.32 V. The blue, brown, green, red, and white spheres represent Co, Fe, Si, O, and H atoms, respectively. Only the topmost atoms are shown for improved clarity.

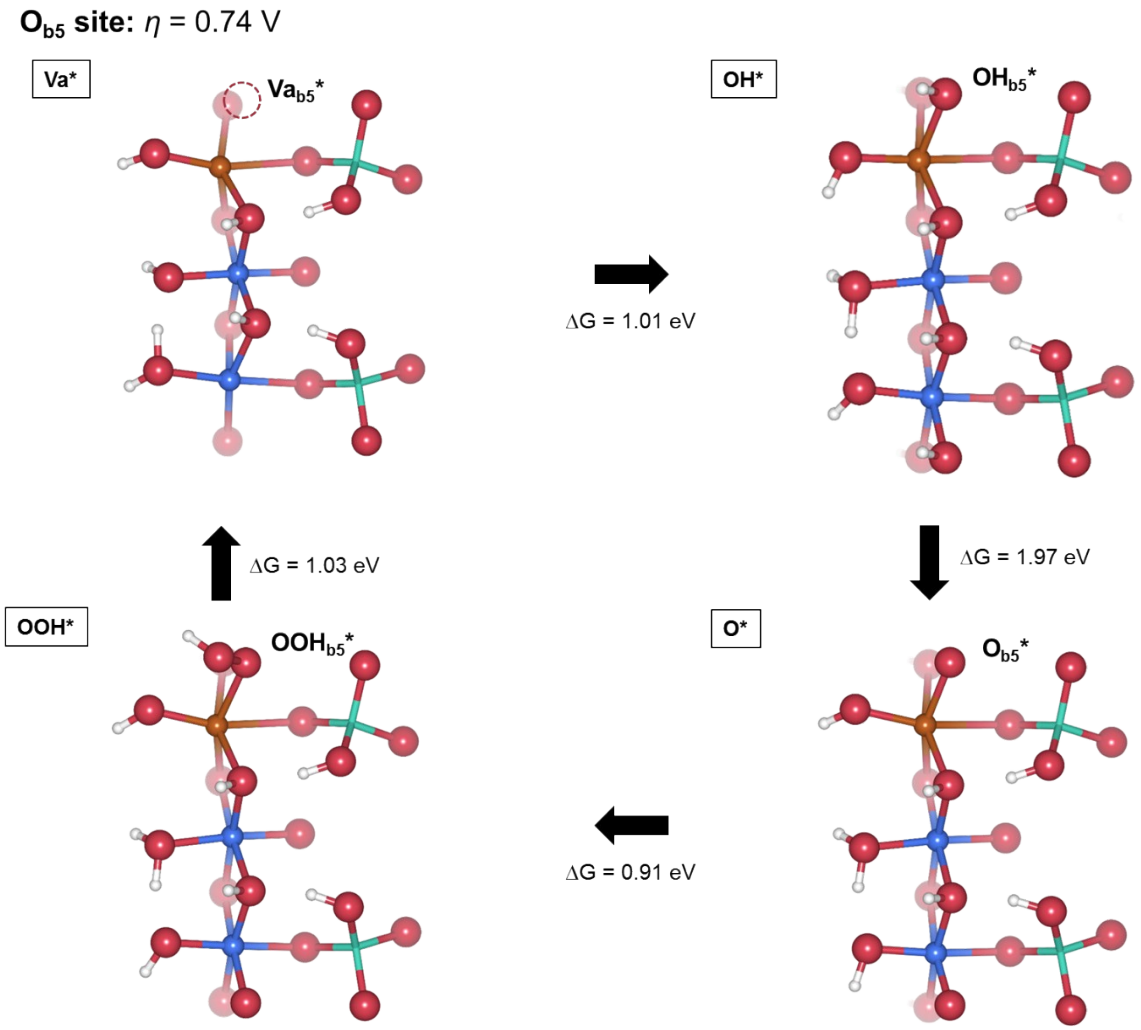

Figure S21. OER pathways and calculated OER energies for bridge site 5 on the Fe-substituted ACP surface (model 2). The PCET step from the OH* to O* state is predicted to be the potential-determining step during the OER cycle for bridge site 5. Thus, the theoretical η estimated for bridge site 5 is 0.74 V. The blue, brown, green, red, and white spheres represent Co, Fe, Si, O, and H atoms, respectively. Only the topmost atoms are shown for improved clarity.

References

1 G. Kresse and J. Furthmüller, *Phys. Rev. B*, 1996, **54**, 11169.
2 S. L. Dudarev, G. A. Botton, S. Y. Savrasov, C. J. Humphreys and A. P. Sutton, *Phys. Rev. B* 1998, **57**, 1505.
3 B. Hammer, L. B. Hansen and J. K. Nørskov, *Phys. Rev. B*, 1999, **59**, 7413.
4 A. Jain, G. Hautier, C. J. Moore, S. Ping Ong, C. C. Fischer, T. Mueller, K. A. Persson and G. Ceder, *Comput. Mater. Sci.*, 2011, **50**, 2295.
5 M. Capdevila-Cortada, Z. Łodziana and N. López, *ACS Catal.*, 2016, **6**, 8370.
6 M. Bajdich, M. García-Mota, A. Vojvodic, J. K. Nørskov and A. T. Bell, *J. Am. Chem. Soc.*, 2013, **135**, 13521.
7 P. Bothra and S. K. Pati, *ACS Energy Lett.*, 2016, **1**, 858.
8 J. S. Kim, I. Park, E.-S. Jeong, K. Jin, W. M. Seong, G. Yoon, H. Kim, B. Kim, K. T. Nam and K. Kang, *Adv. Mater.*, 2017, **29**, 1606893.
9 G. Kresse and D. Joubert, *Phys. Rev. B*, 1999, **59**, 1758.
10 J. K. Nørskov, T. Bligaard, A. Logadottir, S. Bahn, L. B. Hansen, M. Bollinger, H. Bengaard, B. Hammer, Z. Sljivancanin, M. Mavrikakis, Y. Xu, S. Dahl and C. J. H. Jacobsen, *J. Catal.*, 2002, **209**, 275.
11 T. Bligaard, J. K. Nørskov, S. Dahl, J. Matthiesen, C. H. Christensen and J. Sehested, *J. Catal.*, 2004, **224**, 206.
12 A. Vojvodic, F. Calle-Vallejo, W. Guo, S. Wang, A. Toftelund, F. Studt, J. I. Martínez, J. Shen, I. C. Man, J. Rossmeisl, T. Bligaard, J. K. Nørskov and F. Abild-Pedersen, *J. Chem.Phys.*, 2011, **134**, 244509.
13 J. Rossmeisl, Z. W. Qu, H. Zhu, G. J. Kroes and J. K. Nørskov, *J. Electroanal. Chem.*, 2007, **607**, 83.
14 I. C. Man, H.-Y. Su, F. Calle-Vallejo, H. A. Hansen, J. I. Martínez, N. G. Inoglu, J. Kitchin, T. F. Jaramillo, J. K. Nørskov and J. Rossmeisl, *ChemCatChem*, 2011, **3**, 1159.
15 M. W. Kanan and D. G. Nocera, *Science*, 2008, **321**, 1072.
16 G. Nagaraju, Y. H. Ko and J. S. Yu, *CrystEngComm*, 2014, **16**, 11027.
17 W. Zhang, Y. Wu, J. Qi, M. Chen, and R. Cao, *Adv. Energy Mater.*, **7**, 2017, 1602547.
18 E. Tsuji, A. Imanishi, K. Fukui and Y. Nakato, *Electrochim. Acta.*, 2011, **56**, 2009.
19 R. Subbaraman, D. Tripkovic, K.-C. Chang, D. Strmcnik, A. P. Paulikas, P. Hirunsit, M. Chan, J. Greeley, V. Stamenkovic and N. M. Markovic, *Nat. Mater.*, 2012, **11**, 550.
20 F. Song and X. Hu, *Nat. Commun.*, 2014, **5**, 4477.
21 Z. Zhao, H. Wu, H. He, X. Xu and Y. Jin, *Adv. Funct. Mater.*, 2014, **24**, 4698.
22 C. Dong, X. Yuan, X. Wang, X. Liu, W. Dong, R. Wang, Y. Duan and F. Huang, *J. Mater. Chem. A*, 2016, **4**, 11292.
23 F. Song and X. Hu, *J. Am. Chem. Soc*., 2014, **136**, 16481.
24 M. Li, Y. Xiong, X. Liu, X. Bo, Y. Zhang, C. Han and L. Guo, *Nanoscale*, 2015, **7**, 8920.
25 J. A. Koza, Z. He, A. S. Miller and J. A. Switzer, *Chem. Mater*., 2012, **24**, 3567.
26 J. Landon, E. Demeter, N. İnoğlu, C. Keturakis, I. E. Wachs, R. Vasić, A. I. Frenkel and J. R. Kitchin, *ACS Catal*., 2012, **2**, 1793.
27 J. Suntivich, K. J. May, H. A. Gasteiger, J. B. Goodenough and Y. Shao-Horn, *Science*, 2011, **334**, 1383.
28 J. G. Lee, J. Hwang, H. J. Hwang, O. S. Jeon, J. Jang, O. Kwon, Y. Lee, B. Han and Y.-G. Shul, *J. Am. Chem. Soc*., 2016, **138**, 3541.
29 S. Yagi, I. Yamada, H. Tsukasaki, A. Seno, M. Murakami, H. Fujii, H. Chen, N. Umezawa, H. Abe, N. Nishiyama and S. Mori, *Nat. Commun*., 2015, **6**, 8249.
30 B. Zhang, X. Zheng, O. Voznyy, R. Comin, M. Bajdich, M. García-Melchor, L. Han, J. Xu, M. Liu, L. Zheng, F. P. G. de Arquer, C. T. Dinh, F. Fan, M. Yuan, E. Yassitepe, N. Chen, T.

Regier, P. Liu, Y. Li, P. D. Luna, A. Janmohamed, H. L. Xin, H. Yang, A. Vojvodic and E. H. Sargent, *Science* 2016, **352**, 333.